Relativistic high-order harmonic generation of spatiotemporal optical vortices

Zi-Yu Chen,* Ronghao Hu,† Sen Zhang, and Tingfei Yuan
Key Laboratory of High Energy Density Physics and Technology (MoE), College of Physics, Sichuan University, Chengdu 610064, China

(Received 13 October 2021; revised 27 June 2022; accepted 6 July 2022; published 18 July 2022)

It is well known that light can possess spin angular momentum (SAM) and orbital angular momentum (OAM) in the longitudinal direction. Interesting novel light with transverse SAM or OAM has also been discovered recently, with the latter being called spatiotemporal optical vortices. Here we present a route to generate spatiotemporal optical vortices by means of high harmonic generation from relativistic laser plasma interactions. Three-dimensional particle-in-cell simulations show the evidence of edge dislocations in wave front structures and circulating energy flow in space-time. Further calculations of the SAM, OAM and total angular momentum confirm the harmonics carrying pure transverse OAM with noninteger values. The results open up a possibility to generate intense spatiotemporal optical vortices in the extreme ultraviolet region with attosecond duration.

DOI: 10.1103/PhysRevA.106.013516

I. INTRODUCTION

It has long been known that light or an electromagnetic wave carries not only linear momentum but also angular momentum. Speculated by Poynting in 1900s [1] and then detected by Beth in 1930s [2], circularly polarized light possesses angular momentum, which we now know is associated with the spin angular momentum (SAM) of light. Each photon of a circularly polarized light carries a SAM value of $\pm\hbar$ with $\hbar$ the reduced Planck constant and the SAM direction is either parallel or antiparallel to the beam axis.

In 1970s, Nye and Berry introduced the concept of dislocations [3], including screw, edge, and mixed edge-screw dislocations, analogous to those in imperfect crystal lattice, to wave front in optics and implied the formation of optical vortices. While screw wave front dislocations only have vortex lines parallel to the wave propagation direction, edge and mixed edge-screw dislocations can have vortex lines orthogonal to the propagation direction. In 1992, Allen *et al.* pointed out that Laguerre-Gaussian (LG) beams exhibit screw dislocations in wave fronts with a helical shape and thus belong to optical vortices that carry orbital angular momentum (OAM) [4]. The OAM value per photon of LG beams is quantized and equal to the topological charge in units of $\hbar$, with OAM direction also aligned with the beam axis [5]. Thus the well-known SAM of circularly polarized beams and OAM of LG beams are both longitudinal, i.e., aligned with the direction of mean momentum.

In the last decade, optical fields with transverse angular momentum, i.e., angular momentum direction orthogonal to the wave propagation direction, have attracted rising interest [6]. Light with transverse SAM has electric-field vector spinning around an axis perpendicular to the propagation plane, analogy to a photonic wheel [7]. Transverse SAM of light has been identified to emerge from several processes, such as in evanescent waves [8–12], focused beams [13–15], interference fields [16], bianisotropic media [17], and even in unpolarized light [18]. Recently, existence of vortex light beams with transverse OAM was also predicted possible [19] and later discovered experimentally by several groups [20–24]. This novel feature of optical pulse opens new opportunities in various fields. The transverse OAM can be generated by edge or mixed edge-screw phase dislocations in polychromatic beams [25]. Light beams with transverse OAM are also called spatiotemporal optical vortices (STOV), since the local electromagnetic energy is spiral in the plane coupling the spatial and temporal profiles. While this optical phenomenon is fascinating, the method so far to generate such STOV with purely transverse OAM is limited. The reported results mainly concern about the visible spectral region. Lately, STOV in the extreme ultraviolet regime has been reported from STOV-laser-driven gas harmonics [26]. Still, it is challenging to generate short-wavelength STOV with high intensity from non-STOV driving lasers.

In this work, we present the generation of an alternative type of intense ultrashort STOV from laser plasma interactions through three-dimensional (3D) particle-in-cell (PIC) simulations. When a relativistically intense laser vector beam with radial polarization obliquely incident onto a solid-plasma surface, the reflected intense high harmonics are demonstrated to be STOV carrying pure transverse OAM with noninteger values. The underlying physical origin is revealed and attributed to transverse gradients of field phase as a result of vector beams at oblique incidence.

II. SIMULATION SETUP

We perform the 3D PIC simulations using the code VLPL (Virtual Laser Plasma Lab) [27]. A radially polarized laser pulse is obliquely incident onto a solid-plasma surface. The initial propagation direction is along the x axis. The incidence angle is 45°. Thus the reflected pulse propagates along the

*ziyuch@scu.edu.cn
†ronghaohu@scu.edu.cn

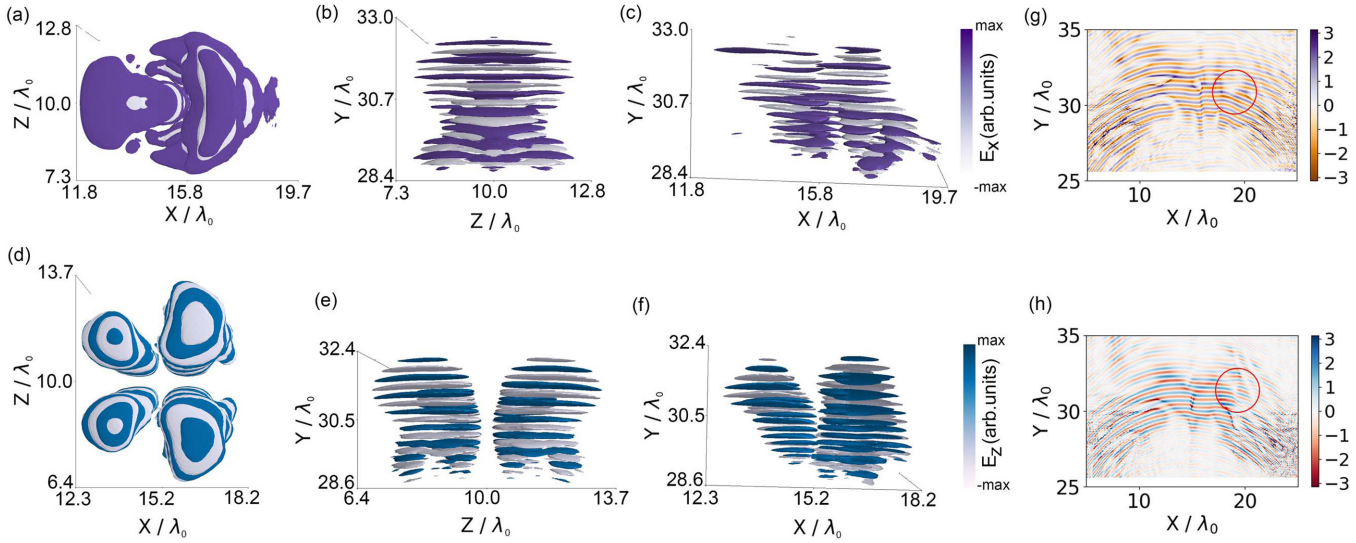

FIG. 1. Wave front and phase structures of the reflected second harmonics in different spatial planes. The first and second rows of panels (a)–(f) correspond to isosurfaces of the transverse electric fields E_x and E_z, respectively. Panels (g) and (h) are the total phase profiles (including the spatiotemporal winding phase and propagation phase terms) of the fields correspond to panels (c) and (f) at $z = 0$, respectively. In the spatiotemporal x-y plane, the isosurfaces display edge dislocation structures and the total phases exhibit characteristic fork grating structures (highlighted in the red circles).

y axis. The interaction scheme is shown in Appendix A. The laser wavelength is $\lambda_0 = 800$ nm. The normalized laser amplitude is $a_0 = eE_0/m_e\omega_0 c = 20$, corresponding to an intensity of about 8×10^{20} W/cm^2, where E_0 is the laser amplitude, ω_0 is the laser angular frequency, c is the light speed in vacuum, e and m_e are elementary charge and electron mass, respectively. The laser has a Gaussian temporal profile with pulse duration of about 6.7 fs. The laser spot size is about $2\lambda_0$. The method to generate the radially polarized pulse in the simulations has been described and tested in Ref. [28]. The fully ionized plasma with immobile ions has an electron density of $10n_c$ and thickness of $0.5\lambda_0$, where $n_c = \epsilon_0 m_e \omega_0^2/e^2$ is the critical plasma density for laser frequency ω_0 and ϵ_0 is the permittivity of free space. A preplasma region exists in the front of the plasma slab with an exponential density profile. The density scale length is $L_s = 0.1\lambda_0$. The simulation box size is $X \times Y \times Z = 25\lambda_0 \times 35\lambda_0 \times 20\lambda_0$. The grid step size is $\Delta x \times \Delta y \times \Delta z = \lambda_0/40 \times \lambda_0/40 \times \lambda_0/40$. Each cell is filled with six macroparticles. Absorption boundary condition is used for both fields and particles.

III. RESULTS AND DISCUSSION

As studied before, the reflected field contains high-order harmonics due to the relativistically oscillating plasma mirror mechanism [28], which supports the synthesis of ultrashort pulses with attosecond duration. Here we mainly select the second-harmonic fields for the purpose of demonstration. Figure 1 shows the isosurfaces of the transverse electric fields E_x and E_z after spectral filtering in the frequency range $[1.5\omega_0, 2.5\omega_0]$ in different spatial planes. One notable feature is that the patterns of both E_x and E_z in the x-z and y-z plane exhibit axial symmetry while nonaxisymmetry in the x-y plane (i.e., the spatiotemporal plane). More importantly, the isosurfaces of both E_x and E_z in the x-y plane show evident edge dislocation structures. In comparison, the fields in the x-z and y-z planes do not show any structures of screw, edge, or mixed edge-screw dislocations. As first pointed out in the seminal paper by Nye and Berry [3], such edge dislocations may lead to singular optical fields, implying that transverse optical vortices may exist in the x-y plane. Figures 1(g) and 1(h) show the total phase distributions in the spatiotemporal x-y plane for electric fields E_x and E_z at $z = 0$, respectively. Here, the total phase $\varphi_{\rm tot}$ contains the contributions of spatiotemporal phase term $\varphi_{\rm st}$ and propagation phase term $\mathbf{k} \cdot \mathbf{r}$ ($\mathbf{k}$ is the wave vector). As the complexity of the reflected pulse (e.g., nonuniform polarization and divergent propagation directions), the spatiotemporal phase $\varphi_{\rm st}$ is difficult to extract accurately. Nevertheless, the characteristic fork grating structures in the total phase can be observed clearly, which is a signature of optical vortices.

The electromagnetic energy of STOV would circulate in the space-time plane upon wave propagation. Figure 2 shows the distribution of wave energy density $\mathcal{W}$ of the second harmonics in different spatial planes at two temporal instants, i.e., $t = 22T_0$ [see Figs. 2(d)–2(f)] and $t = 24T_0$ [see Figs. 2(a)–2(c)]. Here,

$$\mathcal{W} = \frac{1}{2}\left(\epsilon_0 E^2 + \frac{1}{\mu_0} B^2\right), \tag{1}$$

E and B are the electric and magnetic fields respectively, and μ_0 is the permeability of free space. Notably, in the x-y plane, transverse shift of wave energy density distribution can be clearly seen from the areas in the green circles of Figs. 2(c) and 2(f). While in the x-z and y-z planes, no *net* flow of wave energy density can be evidently observed due to the symmetric energy distribution. The circulating energy flow in the x-y plane as a function of time represents another important evidence that the reflected harmonic fields are STOV.

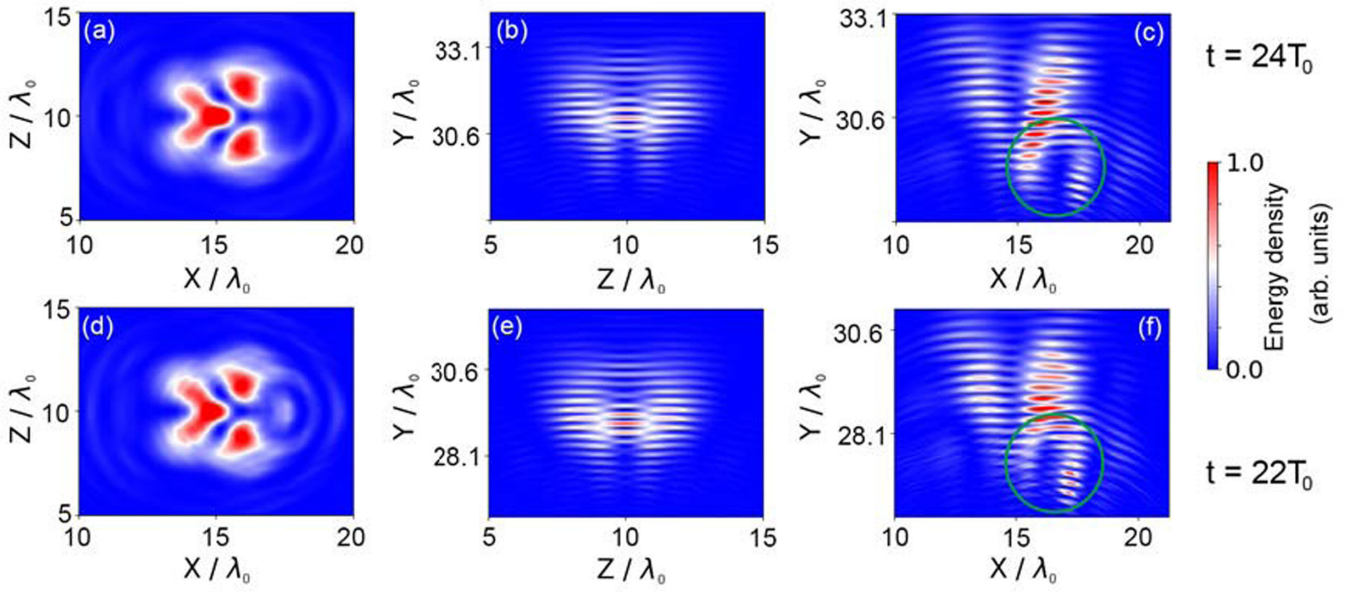

FIG. 2. Spatial distribution of wave energy density of the second harmonics. The data of first and second row are recorded at two different time instants. The first to third columns correspond to data in different spatial planes. The green circles in panels (c) and (f) spotlight the asymmetric spatial distribution and circulating energy flow in the spatiotemporal x-y plane.

To further confirm the harmonic fields being STOV carrying nonzero transverse OAM, we next directly calculate the values of angular momentum (including SAM, OAM, and total angular momentum, i.e., TAM) of the high harmonics using the electric (**E**) and magnetic (**B**) field data obtained from the PIC simulations. The expressions for calculation are as follows. The TAM of an electromagnetic field can be expressed as [29]

$$\mathbf{J} = \int (\mathbf{r} \times \mathbf{p}) d\mathbf{r} = \epsilon_0 \int \mathbf{r} \times (\mathbf{E} \times \mathbf{B}) d\mathbf{r}, \tag{2}$$

where $\mathbf{r} = x\hat{\mathbf{e}}_x + y\hat{\mathbf{e}}_y + z\hat{\mathbf{e}}_z$ is the position vector with $\hat{\mathbf{e}}_x$, $\hat{\mathbf{e}}_y$, and $\hat{\mathbf{e}}_z$ being unit vectors and $\mathbf{p} = \epsilon_0 \mathbf{E} \times \mathbf{B}$ is the linear momentum density. Inserting $\mathbf{B} = \nabla \times \mathbf{A}$ with $\mathbf{A}$ being the vector potential into the right-hand term of Eq. (2), the TAM can be separated into two parts as $\mathbf{J} = \mathbf{S} + \mathbf{L}$ with [30]:

$$\mathbf{S} = \epsilon_0 \int (\mathbf{E} \times \mathbf{A}) d\mathbf{r}, \tag{3}$$

and

$$\mathbf{L} = \epsilon_0 \sum_{i=x,y,z} \int \left[E^i (\mathbf{r} \times \nabla) \mathbf{A}^i \right] d\mathbf{r}, \tag{4}$$

where Eq. (3) (**S**) is associated with the SAM and Eq. (4) (**L**) with the OAM of the field. Furthermore, the vector potential **A** can be computed by the magnetic field **B** through

$$\nabla \times \mathbf{B} = \nabla \times (\nabla \times \mathbf{A}) = -\nabla^2 \mathbf{A}, \tag{5}$$

where Coulomb gauge $\nabla \cdot \mathbf{A} = 0$ is used. Through Fourier transform approach with respect to Eq. (5), the vector potential can then be calculated as [31]

$$\mathbf{A} = \mathcal{F}^{-1}\{i\mathbf{k} \times \mathcal{F}\{\mathbf{B}\}/k^2\}, \tag{6}$$

where $\mathcal{F}$ and $\mathcal{F}^{-1}$ denote Fourier transform and inverse Fourier transform, respectively. Finally, since the total electromagnetic field energy can be obtained as $W = \int \mathcal{W} d^3 r$, the values of TAM, SAM, and OAM per photon can then be calculated as $\mathbf{J}/W$, $\mathbf{S}/W$, and $\mathbf{L}/W$, respectively.

We note there was some controversial before [32–34] with respect to the physical meaning of separating the TAM of an electromagnetic field into contributions of a SAM and an OAM part as Eq. (2). We first calculate the SAM and OAM values of some typical Gaussian beams based on Eq. (2) numerically and compare them to the theoretically known values, which is also a good test of the separation's physical validity. It should also be noted that the TAM and OAM are dependent on the choice of the coordinate origin. Here we take the coordinate origin of the position vector as the center of wave energy of the beam:

$$\mathbf{r}_o = \frac{\int \mathbf{r} \mathcal{W} d^3 r}{\int \mathcal{W} d^3 r}, \tag{7}$$

the justification of which is verified by the correctness of calculated SAM and OAM values of the known beams.

Figure 3 shows the calculation results of TAM, SAM, and OAM values per photon using the expressions aforementioned for several typical beams generated in the 3D PIC simulations. Figures 3(a)–3(c) correspond to laser pulses propagating along the x direction. Linearly polarized (LP) pulses carry zero SAM and OAM and the calculated results shown in Fig. 3(a) give exactly the same values. Left-handed circularly polarized (LCP) photon only have SAM with $S_x = -1\hbar = J_x$ in the longitudinal direction, while right-handed circularly polarized (RCP) photon only have SAM with $S_x = 1\hbar = J_x$ in the longitudinal opposite direction, which are also well reproduced in the calculation results shown in Figs. 3(b) and 3(c), respectively. Figures 3(b)–3(f) correspond respectively to the fundamental (H1), second (H2), and third harmonic (H3) fields propagating along the y direction generated by

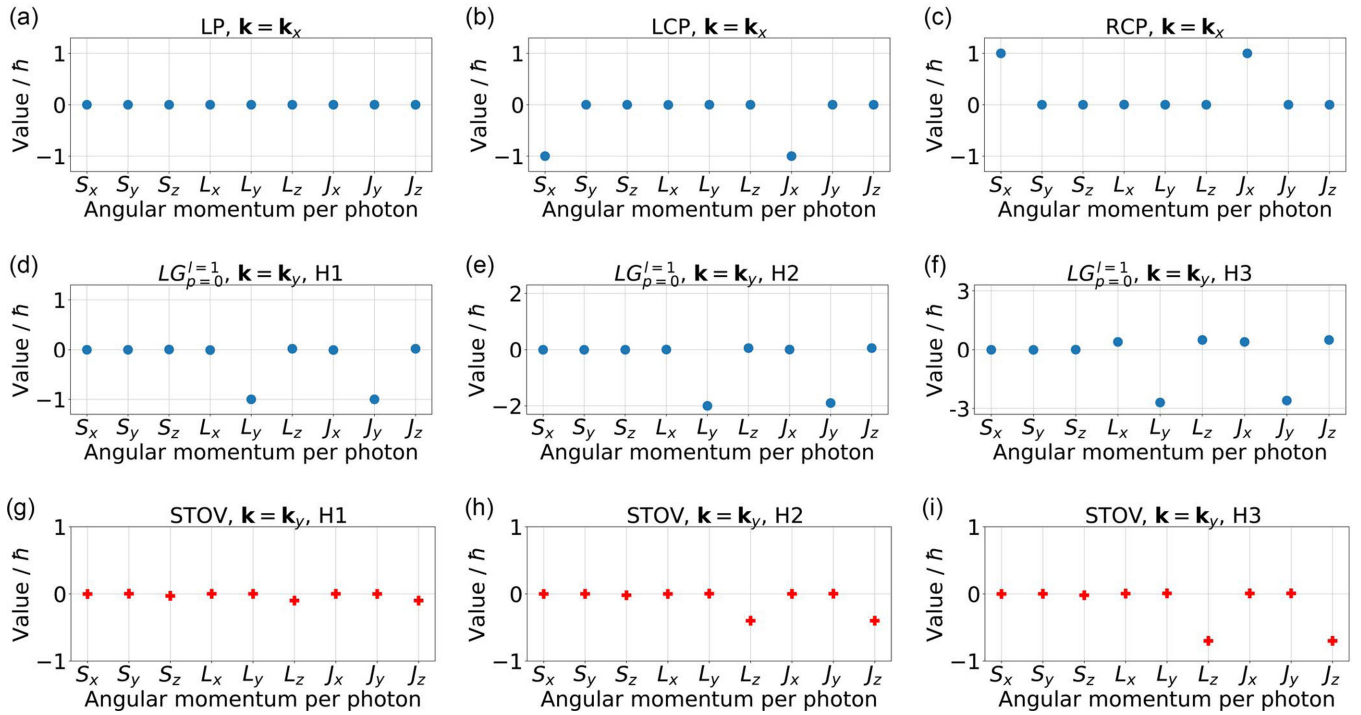

FIG. 3. Calculation of the spin angular momentum (S), orbital angular momentum (L), and total angular momentum (J) per photon for different electromagnetic pulses generated in the 3D PIC simulations: (a) Linearly polarized (LP) laser; (b) Left-handed circularly polarized (LCP) laser; (c) Right-handed circularly polarized (RCP) laser; (d) Fundamental frequency (H1), (e) second harmonic (H2), and (f) third harmonic (H3) of the reflected fields driven by a linearly polarized Laguerre-Gaussian (LG) pulse with radial index $p = 0$ and azimuthal index $l = 1$ under oblique incidence; (g) H1, (h) H2, and (i) H3 of the reflected fields (STOV) driven by the radially polarized laser vector beams under oblique incidence. $\mathbf{k}$ is the wave vector.

a linearly polarized LG pulse (with radial index $p = 0$ and azimuthal index $l = 1$) reflected from a plasma surface with 45° incidence angle. The reflected harmonic fields are also LG pulses with azimuthal index scaling with its order [35]. Then the H1, H2, and H3 photons should carry OAM with $L_y = -1\hbar$, $-2\hbar$, and $-3\hbar$, respectively, which again agree with the calculation values shown in Figs. 3(b)–3(f). Note the small nonzero values of L_z and L_x for H3 in Fig. 3(f), which may be attributed to out-of-plane and in-plane angular transverse shift of vortex light reflection due to OAM Hall effect of photons [36–39]. The effect is small and increases with the OAM value. These calculation results ambiguously demonstrate our method can compute the TAM, SAM, and OAM values of the simulated fields quite accurately. The results also bring the first numerical test to the issue under debate of the separation of TAM into SAM and OAM as Eqs. (2)–(4).

Having benchmarked the method, now we can apply it to calculate the momentum values of the harmonic fields driven by the radially polarized laser pulse. The calculation results for the H1, H2, and H3 fields are shown in Figs. 3(g)–3(i), respectively. The detailed numbers of all calculated angular-momentum values are provided in Appendix B. Clearly, all values of the angular-momentum components are zero except for L_z, which is approximately equal to J_z. Since OAM in the z direction represents vortices in the x-y plane, this calculation result is consistent with the field structures in Figs. 1 and 2, where only the fields in the x-y plane show edge dislocations and in-plane flow of wave energy distributions. The calculated OAM values L_z per photon are $L_z^1 \approx -0.16\hbar$, $L_z^2 \approx -0.41\hbar$, $L_z^3 \approx -0.67\hbar$, $L_z^4 \approx -0.75\hbar$, $L_z^5 \approx -1.1\hbar$ for each harmonic order, respectively. These numerical results are approximately in accordance with the conservation rule of transverse OAM [23,26], i.e., the OAM of qth order harmonic is q times that of the fundamental frequency, as displayed in Fig. 4. Here, the transverse OAM values are fractions instead of integers. Hancock *et al.* addressed noninteger OAM values recently and showed that the OAM of STOV is dependent on ratio of spatial and temporal scales of the winding [40]. Besides, our

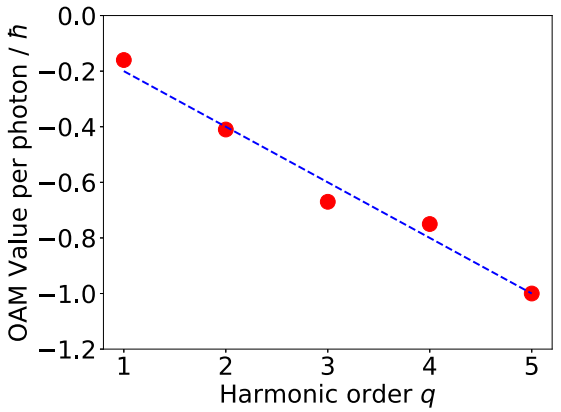

FIG. 4. The calculated OAM values L_z per photon for each order of harmonic. The red dots are the calculated values. The dashed blue line is a linear fit of the calculated values.

calculated OAM value is close to zero if a narrow bandwidth spectral filtering is performed (see Appendix C for details). This is in agreement with STOV supported by polychromatic pulses [19]. These calculation results lend additional crucial support to the generated harmonic fields being STOV that carry pure nonzero transverse OAM.

A physical insight underlying the nonzero transverse OAM generation can be gained by analyzing the time-averaged optical torque density Γ generated by the radially polarized light obliquely incident on the plasma surface. Generally, we have [24,41]

$$\Gamma \propto \mathrm{Re}\{\mathbf{D}^* \times \mathbf{E}\} \propto \mathrm{Re}\{\mathbf{E}_x^* \times \mathbf{E}_\tau\}, \tag{8}$$

where $\mathbf{D}$ is the electric displacement field, τ refers to the transverse field components, $\mathrm{Re}\{\cdot\}$ refers to the real part, and $(\cdot)^*$ denotes the complex conjugate. Considering $\mathbf{E} = \mathbf{A}(x, y, z)e^{i(kx-\omega t)}$ and the local Gauss law, the expression relating the longitudinal field amplitude with the transverse one can be obtained as [41]

$$A_x = \frac{i}{k}\frac{\partial |A_\tau|}{\partial \tau}e^{i\phi_\tau} - \frac{1}{k}\frac{\partial \phi_\tau}{\partial \tau}|A_\tau|e^{i\phi_\tau}, \tag{9}$$

where $A_\tau = |A_\tau|e^{i\phi_\tau}$ with ϕ_τ being the phase for the transverse components. Note longitudinal electric fields play important roles in the effect. Favorably, radially polarized beams have strong longitudinal electric fields with tight focus. Then we can get the transverse torque density as

$$\Gamma_{\tau'} \propto \mathrm{Re}\{\mathbf{E}_x^* \times \mathbf{E}_\tau\} \propto \left(\frac{\partial \phi_\tau}{\partial \tau}\right)|A_\tau|^2 \hat{\mathbf{e}}_x \times \hat{\mathbf{e}}_\tau. \tag{10}$$

We see the transverse torque requires phase gradients to be present in the transverse field components. Recall that the transverse field of radially polarized pulse is locally linear polarization with field vector orientation varying azimuthally. As such, the local transverse gradient of field amplitude is zero but the transverse gradient of field phase is nonzero. This further explains why vector beams are needed while normal Gaussian beams do not lead to transverse OAM [see, e.g., the results by linearly polarized LG pulses shown in Figs. 3(d)–3(f)].

In addition, with oblique incidence in the x-y plane, the interaction geometry is symmetric in the z direction while asymmetric in the y direction. As a result, the transverse phase gradients in the z direction at different locations are equal in magnitude but opposite in sign, and thus the total net phase gradient in space $\int(\partial\phi_z/\partial z)d^3r = 0$. Then the total torque in the y direction $\int \Gamma_y d^3r \propto \int \mathrm{Re}\{E_x^* E_z\}dV \propto \int(\partial\phi_z/\partial z)|A_z|^2 d^3r = 0$, since $|A_z|$ also has an axial symmetry. In comparison, the total phase gradient $\int(\partial\phi_y/\partial y)d^3r$ in the asymmetric y direction is nonzero. Therefore, this explains why only a net transverse OAM in the z direction L_z exists, as it is opposite to the torque $\int \Gamma_z d^3r \propto \int \mathrm{Re}\{E_x^* E_y\}d^3r \propto \int(\partial\phi_y/\partial y)|A_y|^2 d^3r \neq 0$. It is the combination of vector beam and oblique incidence that is essential for the nonvanishing cross-effect between the longitudinal and transverse field components and the total transverse phase gradient, which eventually leads to the transverse optical torque and OAM.

It is interesting to note that a recent study by El Ketara *et al.* show that a radially polarized wave obliquely propagating through a uniaxial liquid crystal with respect to the optic axis can give rise to a nonvanishing transverse OAM [24]. We mention that in a previous work we have demonstrated the plasma medium under laser oblique incidence can be equivalently viewed as a uniaxial medium [42]. It is surprising that these two seemingly unrelated systems share a similar underlying physical mechanism in transverse torque and OAM generation.

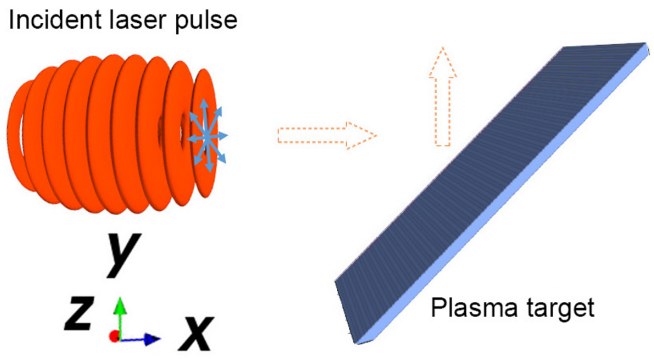

FIG. 5. A sketch of the interaction scheme.

IV. CONCLUSIONS

In conclusion, we numerically demonstrate the generation of an alternative type of STOV carrying pure transverse OAM with noninteger values. Evidence of transverse OAM is observed as edge dislocations in wave front structures and energy flow and redistribution upon propagation. The values of SAM, OAM, and TAM per photon are calculated accurately by separating the spin and orbital part of the TAM, which further confirm the reflected harmonics indeed carrying pure transverse fractional OAM. The underlying physical mechanism can be attributed to the transverse phase gradients of vector beams at oblique incidence. This study presents new opportunities to generate bright STOV extending to the extreme ultraviolet short wavelength with attosecond temporal duration and high intensity, which may lead to a number of applications, such as novel optical manipulation [24] and

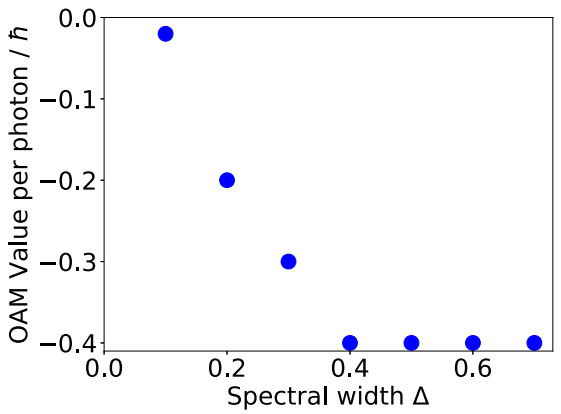

FIG. 6. The calculated transverse OAM value L_z per photon for the second-harmonic order as a function of window width Δ for spectral filtering.

TABLE I. Detailed calculation results of SAM, OAM, and TAM values per photon for each order of harmonic.

	H1	H2	H3	H4	H5
S_x	−0.0014967	−0.0015433	−0.0019142	−0.0026967	−0.0039960
S_y	0.0014759	−0.00041009	0.0011946	0.0019493	0.00049939
S_z	−0.031934	−0.022983	−0.023609	−0.030091	−0.028340
L_x	0.0043135	0.0065273	0.015226	0.038258	0.044867
L_y	0.0015601	0.0047204	0.0051472	0.019835	0.023729
L_z	−0.15751	−0.40942	−0.66675	−0.75498	−1.05848
J_x	0.0026635	0.0061163	0.016533	0.039401	0.045902
J_y	0.00094326	0.0037961	0.0061753	0.024282	0.024320
J_z	−0.17763	−0.41292	−0.66677	−0.77049	−1.07649

topological photonics [6] with high spatial and temporal resolution.

ACKNOWLEDGMENTS

This work was supported in part by the National Natural Science Foundation of China (12175157), National Key Laboratory of Shock Wave and Detonation Physics (JCKYS2020212015), and the Fundamental Research Funds for the Central Universities (YJ202025).

APPENDIX A: INTERACTION SCHEME

We show the sketch of the interaction scheme in Fig. 5. In our simulations, the plasma target surface is tilted at an angle of 45° away from the x or y axis. The incident laser propagates from the left of the simulation box along the x axis. Thus the laser incidence angle is 45° and the reflected pulse propagates along the y axis.

APPENDIX B: DETAILED ANGULAR MOMENTUM VALUES

This Appendix shows the detailed calculation results of angular-momentum values, including SAM (**S**), OAM (**L**), and TAM (**J**) per photon, for each harmonic order of the reflected fields driven by the obliquely incident radially polarized laser pulses upon plasma surfaces, as shown in Table I. The calculations of **S**, **L**, and **J** are based on the expressions given by Eqs. (2)–(4), respectively.

APPENDIX C: EFFECT OF WINDOW WIDTH FOR SPECTRAL FILTERING

Spectral filtering of the qth harmonic order is performed in the frequency range from $q - \Delta$ to $q + \Delta$. When $\Delta = 0.1$, the calculated transverse OAM value L_z is close to zero. L_z increases with window width Δ and stables when $\Delta \geqslant 0.4$, as can be seen in Fig. 6. This result is in accordance with STOV supported by polychromatic pulses.

[1] J. H. Poynting, The wave motion of a revolving shaft, and a suggestion as to the angular momentum in a beam of circularly polarised light, Proc. Roy. Soc. A **82**, 560 (1909).
[2] R. A. Beth, Mechanical detection and measurement of the angular momentum of light, Phys. Rev. **50**, 115 (1936).
[3] J. F. Nye, M. V. Berry, and F. C. Frank, Dislocations in wave trains, Proc. Roy. Soc. A **336**, 165 (1974).
[4] L. Allen, M. W. Beijersbergen, R. J. C. Spreeuw, and J. P. Woerdman, Orbital angular momentum of light and the transformation of Laguerre-Gaussian laser modes, Phys. Rev. A **45**, 8185 (1992).
[5] Y. Shen, X. Wang, Z. Xie, C. Min, X. Fu, Q. Liu, M. Gong, and X. Yuan, Optical vortices 30 years on: oam manipulation from topological charge to multiple singularities, Light: Sci. Appl. **8**, 90 (2019).
[6] K. Y. Bliokh and F. Nori, Transverse and longitudinal angular momenta of light, Phys. Rep. **592**, 1 (2015).
[7] A. Aiello, P. Banzer, M. Neugebauer, and G. Leuchs, From transverse angular momentum to photonic wheels, Nat. Photonics **9**, 789 (2015).
[8] K. Y. Bliokh and F. Nori, Transverse spin of a surface polariton, Phys. Rev. A **85**, 061801(R) (2012).
[9] K.-Y. Kim, I.-M. Lee, J. Kim, J. Jung, and B. Lee, Time reversal and the spin angular momentum of transverse-electric and transverse-magnetic surface modes, Phys. Rev. A **86**, 063805 (2012).
[10] K. Y. Bliokh, A. Y. Bekshaev, and F. Nori, Extraordinary momentum and spin in evanescent waves, Nat. Commun. **5**, 3300 (2014).
[11] K.-Y. Kim and A. X. Wang, Spin angular momentum of surface modes from the perspective of optical power flow, Opt. Lett. **40**, 2929 (2015).
[12] Z. Shao, J. Zhu, Y. Chen, Y. Zhang, and S. Yu, Spin-orbit interaction of light induced by transverse spin angular momentum engineering, Nat. Commun. **9**, 926 (2018).
[13] M. Neugebauer, T. Bauer, A. Aiello, and P. Banzer, Measuring the Transverse Spin Density of Light, Phys. Rev. Lett. **114**, 063901 (2015).
[14] T. Bauer, M. Neugebauer, G. Leuchs, and P. Banzer, Optical Polarization Möbius Strips and Points of Purely Transverse Spin Density, Phys. Rev. Lett. **117**, 013601 (2016).
[15] M. Neugebauer, J. S. Eismann, T. Bauer, and P. Banzer, Magnetic and Electric Transverse Spin Density of Spatially Confined Light, Phys. Rev. X **8**, 021042 (2018).

[16] A. Y. Bekshaev, K. Y. Bliokh, and F. Nori, Transverse Spin and Momentum in Two-Wave Interference, Phys. Rev. X **5**, 011039 (2015).

[17] L. Peng, L. Duan, K. Wang, F. Gao, L. Zhang, G. Wang, Y. Yang, H. Chen, and S. Zhang, Transverse photon spin of bulk electromagnetic waves in bianisotropic media, Nat. Photonics **13**, 878 (2019).

[18] J. S. Eismann, L. H. Nicholls, D. J. Roth, M. A. Alonso, P. Banzer, F. J. Rodríguez-Fortuño, A. V. Zayats, F. Nori, and K. Y. Bliokh, Transverse spinning of unpolarized light, Nat. Photonics **15**, 156 (2021).

[19] K. Y. Bliokh and F. Nori, Spatiotemporal vortex beams and angular momentum, Phys. Rev. A **86**, 033824 (2012).

[20] N. Jhajj, I. Larkin, E. W. Rosenthal, S. Zahedpour, J. K. Wahlstrand, and H. M. Milchberg, Spatiotemporal Optical Vortices, Phys. Rev. X **6**, 031037 (2016).

[21] S. W. Hancock, S. Zahedpour, A. Goffin, and H. M. Milchberg, Free-space propagation of spatiotemporal optical vortices, Optica **6**, 1547 (2019).

[22] A. Chong, C. Wan, J. Chen, and Q. Zhan, Generation of spatiotemporal optical vortices with controllable transverse orbital angular momentum, Nat. Photonics **14**, 350 (2020).

[23] S. W. Hancock, S. Zahedpour, and H. M. Milchberg, Second-harmonic generation of spatiotemporal optical vortices and conservation of orbital angular momentum, Optica **8**, 594 (2021).

[24] M. El Ketara, H. Kobayashi, and E. Brasselet, Sensitive vectorial optomechanical footprint of light in soft condensed matter, Nat. Photonics **15**, 121 (2021).

[25] K. Y. Bliokh, Spatiotemporal Vortex Pulses: Angular Momenta and Spin-Orbit Interaction, Phys. Rev. Lett. **126**, 243601 (2021).

[26] Y. Fang, S. Lu, and Y. Liu, Controlling Photon Transverse Orbital Angular Momentum in High Harmonic Generation, Phys. Rev. Lett. **127**, 273901 (2021).

[27] A. Pukhov, Three-dimensional electromagnetic relativistic particle-in-cell code VLPL (Virtual Laser Plasma Lab), J. Plasma Phys. **61**, 425 (1999).

[28] Z.-Y. Chen and R. Hu, Intense high-order harmonic vector beams from relativistic plasma mirrors, Phys. Rev. A **103**, 023507 (2021).

[29] J. D. Jackson, *Classical Electrodynamics*, 3rd ed. (Wiley, New York, 1998).

[30] *The Angular Momentum of Light*, edited by D. L. Andrews and M. Babiker, (Cambridge University Press, Cambridge, 2012).

[31] Y. Ma, D. Seipt, A. E. Hussein, S. Hakimi, N. F. Beier, S. B. Hansen, J. Hinojosa, A. Maksimchuk, J. Nees, K. Krushelnick, A. G. R. Thomas, and F. Dollar, The effects of laser polarization and wavelength on injection dynamics of a laser wakefield accelerator, Phys. Plasmas **28**, 063101 (2021).

[32] S. J. v. Enk and G. Nienhuis, Spin and orbital angular momentum of photons, Europhys. Lett. **25**, 497 (1994).

[33] S. M. Barnett, Rotation of electromagnetic fields and the nature of optical angular momentum, J. Mod. Opt. **57**, 1339 (2010).

[34] R. P. Cameron, S. M. Barnett, and A. M. Yao, Optical helicity, optical spin and related quantities in electromagnetic theory, New J. Phys. **14**, 053050 (2012).

[35] X. Zhang, B. Shen, Y. Shi, X. Wang, L. Zhang, W. Wang, J. Xu, L. Yi, and Z. Xu, Generation of Intense High-Order Vortex Harmonics, Phys. Rev. Lett. **114**, 173901 (2015).

[36] V. G. Fedoseyev, Spin-independent transverse shift of the centre of gravity of a reflected and of a refracted light beam, Opt. Commun. **193**, 9 (2001).

[37] R. Dasgupta and P. K. Gupta, Experimental observation of spin-independent transverse shift of the centre of gravity of a reflected Laguerre-Gaussian light beam, Opt. Commun. **257**, 91 (2006).

[38] K. Y. Bliokh, Geometrical Optics of Beams with Vortices: Berry Phase and Orbital Angular Momentum Hall Effect, Phys. Rev. Lett. **97**, 043901 (2006).

[39] L. Zhang, B. Shen, X. Zhang, S. Huang, Y. Shi, C. Liu, W. Wang, J. Xu, Z. Pei, and Z. Xu, Deflection of a Reflected Intense Vortex Laser Beam, Phys. Rev. Lett. **117**, 113904 (2016).

[40] S. W. Hancock, S. Zahedpour, and H. M. Milchberg, Mode Structure and Orbital Angular Momentum of Spatiotemporal Optical Vortex Pulses, Phys. Rev. Lett. **127**, 193901 (2021).

[41] F. Cardano and L. Marrucci, Longitudinal fields and transverse rotations, Nat. Photonics **15**, 72 (2021).

[42] Z.-Y. Chen and A. Pukhov, Plasma-based polarization modulator for high-intensity lasers, Phys. Plasmas **23**, 123107 (2016).